INTERNATIONAL JOURNAL FOR NUMERICAL METHODS IN FLUIDS
Int. J. Numer. Meth. Fluids 2005; **49**:975–997
Published online 3 August 2005 in Wiley InterScience (www.interscience.wiley.com). DOI: 10.1002/fld.1034

An eddy viscosity model with near-wall modifications

M. M. Rahman*,† and T. Siikonen‡

Laboratory of Applied Thermodynamics, Department of Mechanical Engineering, Helsinki University of Technology, Sähkömiehentie 4, FIN-02015 HUT, Finland

SUMMARY

An extended version of the isotropic k–ε model is proposed that accounts for the distinct effects of low-Reynolds number (LRN) and wall proximity. It incorporates a near-wall correction term to amplify the level of dissipation in nonequilibrium flow regions, thus reducing the kinetic energy and length scale magnitudes to improve prediction of adverse pressure gradient flows, involving flow separation and reattachment. The eddy viscosity formulation maintains the positivity of normal Reynolds stresses and the Schwarz' inequality for turbulent shear stresses. The model coefficients/functions preserve the anisotropic characteristics of turbulence. The model is validated against a few flow cases, yielding predictions in good agreement with the direct numerical simulation (DNS) and experimental data. Comparisons indicate that the present model is a significant improvement over the standard eddy viscosity formulation. Copyright © 2005 John Wiley & Sons, Ltd.

KEY WORDS: near-wall correction; turbulence anisotropy; realizability; flow separation and reattachment

1. INTRODUCTION

A large number of scientific and engineering calculations adhering to turbulent flows are established on the k–ε model. The standard k–ε model is devised for high Reynolds number turbulent flows and is traditionally used in wall-bounded flows in conjunction with a wall function approach to patch the core region of the flow to the wall region. In this way, the problem of modelling the direct influence of viscosity is avoided. Unfortunately, universal wall functions do not exist in complex flows. Turbulent flows involving boundary layer separation or complex alterations of the surface transport properties represent such examples. It requires the direct integration of the modelled turbulence equations to a solid boundary that plays a crucial role. In particular, predictions of a high Reynolds number turbulence model can be

*Correspondence to: M. M. Rahman, Laboratory of Applied Thermodynamics, Department of Mechanical Engineering, Helsinki University of Technology, Sähkömiehentie 4, FIN-02015 HUT, Finland.
†E-mail: mizanur.rahman@hut.fi
‡E-mail: timo.siikonen@hut.fi

Received 3 March 2005
Revised 10 May 2005
Accepted 12 May 2005

degraded significantly when integrating to a solid boundary without the proper near-wall modifications. Consequently, the near-wall modelling of turbulence has received extensive attention with the bulk of the effort directed toward two-equation models [1–16]. The improvement of low-Reynolds number (LRN) model over the high-Reynolds number model is rooted on the sufficiently resolved turbulence transport processes in the vicinity of the wall.

In a k–ε model approach, the k equation is relatively exact and essentially, the obvious choice is to modify the ε equation for enhancing the predictive capability. However, the modelled dissipation rate equation together with the near-wall correction is not always sufficient to provide the appropriate length scale of turbulence. For instance, the isotropic LRN k–ε eddy viscosity model with a constant C_μ, which is frequently used in computational fluid dynamics, performs quite well for boundary layer flows but fails badly for flows with a high mean shear rate or a massive separation. The possible reasoning is that the eddy viscosity is overpredicted. Basically, an overprediction of the eddy viscosity in the shear flow makes the model dissipative and therefore, causes the separation bubble to shorten. In addition, it violates the realizability constraints: the positivity of the normal Reynolds stresses and Schwarz' inequality between turbulent velocity correlations [17]. In order to improve the ability of the existing k–ε eddy viscosity model in predicting complex turbulent flows, the above-mentioned deficiencies should be removed.

Abandoning the wall function approach to patch near-wall regions, the present study concentrates on near-wall and LRN modifications for the isotropic k–ε model where the integration up to the wall is extremely important. On the way of formulating the near-wall correction term to render the balancing of molecular diffusion, the expansion functions regarding k and ε are deduced in the near-wall region. The near-wall correction augments the dissipation level in nonequilibrium flow regions, thus reducing the turbulent kinetic energy and length scale magnitudes to improve prediction of adverse pressure gradient flows involving separation and reattachment. The wall singularity is removed by using a physically appropriate time scale that never falls below the Kolmogorov (dissipative eddy) time scale, representing time scale realizability enforcement accompanied by the near-wall turbulent phenomena. A near-wall eddy viscosity damping function f_μ is introduced, which satisfies the wall-limiting behaviour and reaches the upper limit value of unity in the logarithmic layer. The turbulent Prandtl numbers $\sigma_{(k,\varepsilon)}$ are adjusted such as to provide substantial turbulent diffusion in near-wall regions. Furthermore, a modified coefficient C_μ that depends nonlinearly on both the rotational and irrotational strains is proposed based on the realizability constraints and appropriate experiments.

To this end, it must be emphasized that compared with other published modifications to the isotropic k–ε model, the present paper has the following attributes. The construction of $C_\mu f_\mu$ reduces the potentiality of $C_\mu f_\mu$ to grow particularly in near-wall regions. In addition, the damping function f_μ contains the invariants of strain rate and vorticity. It is a new feature that is not preserved by many models in the literature. The near-wall correction term with a variable coefficient is determined in a consistent manner, balancing the molecular diffusion in the near-wall region. The turbulence anisotropy is introduced with the model coefficients $\sigma_{(k,\varepsilon)}$. Obviously, the new model extends the ability of the two-equation model to account for nonequilibrium and anisotropic effects.

The performance of the new model is demonstrated through the comparison with experimental and direct numerical simulation (DNS) data of well-documented flows, consisting of a fully developed channel flow, an asymmetric plane diffuser flow and a plane U-duct flow,

respectively. The test cases are selected such as to justify the ability of the model to replicate the combined effects of LRN, near-wall turbulence and nonequilibrium.

2. TURBULENCE MODELLING

The two-dimensional Reynolds-averaged Navier–Stokes (RANS) equations, including the equations for the kinetic energy k and dissipation ε, can be written in the following form:

$$\frac{\partial U}{\partial t} + \frac{\partial (F - F_v)}{\partial x} + \frac{\partial (G - G_v)}{\partial y} = Q \tag{1}$$

where $U = (\rho, \rho u, \rho v, E, \rho k, \rho \varepsilon)^{\mathrm{T}}$. The inviscid fluxes are

$$F = \begin{pmatrix} \rho u \\ \rho u^2 + p + \frac{2}{3}\rho k \\ \rho uv \\ u(E + p + \frac{2}{3}\rho k) \\ \rho uk \\ \rho u\varepsilon \end{pmatrix}, \quad G = \begin{pmatrix} \rho v \\ \rho vu \\ \rho v^2 + p + \frac{2}{3}\rho k \\ v(E + p + \frac{2}{3}\rho k) \\ \rho vk \\ \rho v\varepsilon \end{pmatrix} \tag{2}$$

Here ρ is the density and p is the pressure. The total energy is defined as

$$E = \rho e + \frac{\rho \mathbf{V} \cdot \mathbf{V}}{2} + \rho k \tag{3}$$

where e is the specific internal energy and $\mathbf{V} = u\mathbf{i} + v\mathbf{j}$ is the velocity. The viscous fluxes are

$$F_v = \begin{pmatrix} 0 \\ \tau_{xx} + \frac{2}{3}\rho k \\ \tau_{xy} \\ u\tau_{xx} + v\tau_{xy} - q_x \\ \mu_k(\partial k/\partial x) \\ \mu_\varepsilon(\partial \varepsilon/\partial x) \end{pmatrix}, \quad G_v = \begin{pmatrix} 0 \\ \tau_{xy} \\ \tau_{yy} + \frac{2}{3}\rho k \\ u\tau_{xy} + v\tau_{yy} - q_y \\ \mu_k(\partial k/\partial y) \\ \mu_\varepsilon(\partial \varepsilon/\partial y) \end{pmatrix} \tag{4}$$

and the viscous stress tensor can be given as

$$\tau_{ij} = 2\mu(S_{ij} - \tfrac{1}{3}S_{kk}\delta_{ij}) - \rho\overline{u_i u_j} \tag{5}$$

where μ is the laminar viscosity and the Reynolds stresses $\rho\overline{u_i u_j}$ are related to the mean strain rate tensor S_{ij} through the Boussinesq approximation:

$$-\rho\overline{u_i u_j} = 2\mu_T(S_{ij} - \tfrac{1}{3}S_{kk}\delta_{ij}) - \tfrac{2}{3}\rho k\delta_{ij} \tag{6}$$

The heat flux is calculated from

$$\mathbf{q} = -\left(\mu \frac{c_p}{Pr} + \mu_T \frac{c_p}{Pr_\mathrm{T}}\right)\nabla T \tag{7}$$

where c_p is the specific heat at constant pressure, Pr and Pr_T represent the molecular and turbulent Prandtl numbers, respectively, and T implies the temperature. Clearly, the turbulent part of the total heat flux is estimated using the Boussinesq approximation. The value of Pr_T is chosen to be 0.9 [1]. Since the viscous dissipation presumably dominates near the wall, the turbulent viscosity is evaluated from

$$\mu_T = C_\mu f_\mu \rho k T_t \tag{8}$$

where the dynamic time scale k/ε is replaced by a realizable time scale T_t and f_μ denotes the eddy viscosity damping function. The model coefficient C_μ is in general a scalar function of the invariants formed on the strain rate S_{ij} and vorticity W_{ij} tensors in question [18, 19]:

$$S_{ij} = \frac{1}{2}\left(\frac{\partial u_i}{\partial x_j} + \frac{\partial u_j}{\partial x_i}\right), \quad W_{ij} = \frac{1}{2}\left(\frac{\partial u_i}{\partial x_j} - \frac{\partial u_j}{\partial x_i}\right) \tag{9}$$

The invariants of mean strain rate and vorticity tensors are defined by $S = \sqrt{2S_{ij}S_{ij}}$ and $W = \sqrt{2W_{ij}W_{ij}}$, respectively. The detailed functional form of C_μ is determined relying on the constraints such as realizability and appropriate experiments. The diffusion of turbulence is modelled as

$$\mu_k \nabla k = \left(\mu + \frac{\mu_T}{\sigma_k}\right)\nabla k, \quad \mu_\varepsilon \nabla \varepsilon = \left(\mu + \frac{\mu_T}{\sigma_\varepsilon}\right)\nabla \varepsilon \tag{10}$$

where σ_k and σ_ε are the appropriate turbulent Prandtl numbers. The source term Q for the k and ε equations can be written as

$$Q = \begin{pmatrix} \rho P - \rho\varepsilon \\ \dfrac{C_{\varepsilon 1}\rho P - C_{\varepsilon 2}\rho\varepsilon}{T_t} + \Pi_\varepsilon \end{pmatrix} \tag{11}$$

where the turbulent production term $P = -\overline{u_i u_j}(\partial u_i/\partial x_j)$ and Π_ε is a positive source term designed to balance the molecular diffusion in the near-wall region. The associated empirical constants are: $C_{\varepsilon 1} = 1.44$ and $C_{\varepsilon 2} = 1.83$.

2.1. Model realizability

The new model appears with recourse to the realizability constraints, reflecting physically necessary conditions for developing a compatible turbulence model. The realizability conditions are defined as [17]

$$\overline{u_i^2} \geqslant 0, \quad \frac{\overline{u_i u_j}^2}{\overline{u_i^2}\,\overline{u_j^2}} \leqslant 1 \tag{12}$$

Equation (12) also represents the minimal requirement to prevent a turbulence model from producing nonphysical results. The commonly used isotropic k–ε eddy viscosity model with a

constant $C_\mu = 0.09$ becomes unrealizable in the case of a large mean strain rate parameter $T_t S$ (when $T_t S > 3.7$), producing negative normal stresses and Equation (12) is violated [20]. To ensure realizability, the model coefficient C_μ cannot be a constant. It must be related with the mean flow deformation rate. Accordingly, a new formulation for C_μ as suggested by Gatski and Speziale [19] is adopted:

$$C_\mu = \frac{3(1+\eta^2)\alpha_1}{3+\eta^2+6\eta^2\xi^2+6\xi^2}, \quad \eta = \alpha_2 T_t S, \quad \xi = \alpha_3 T_t W \tag{13}$$

The coefficients α_1–α_3 associated with Equation (13) are given by

$$\begin{aligned} \alpha_1 &= g\left(\tfrac{1}{4} + \tfrac{2}{3}\Pi_b^{1/2}\right), \quad \alpha_2 = \frac{3}{8\sqrt{2}} g \\ \alpha_3 &= \frac{3}{\sqrt{2}}\alpha_2, \quad g = \left(1 + 2\frac{P}{\varepsilon}\right)^{-1} \end{aligned} \tag{14}$$

where $\Pi_b = b_{ij} b_{ij}$ and the anisotropy of the Reynolds stress b_{ij} is defined as

$$b_{ij} = \frac{\overline{u_i u_j}}{2k} - \frac{1}{3}\delta_{ij} \tag{15}$$

To this end, it must be acknowledged that the associated constants are slightly modified to reproduce the data of DNS and experiments.

For homogeneous turbulent flows that are in equilibrium, Π_b and P/ε attain constant values, so that $\Pi_b \approx 0.11$ and $P/\varepsilon = (C_{\varepsilon 2} - 1)/(C_{\varepsilon 1} - 1) \approx 1.9$. These values can be set in Equation (14) to calculate inhomogeneous flows. However, the necessity to account for changes in Π_b and P/ε is appreciable since their equilibrium values drive the model to inconsistency in the context of a mild departure from equilibrium. Girimaji [21] has developed a fully explicit, self-consistent variant of Reference [19] by solving the cubic equation for P/ε. Nevertheless, the resulting solution for P/ε is unfortunately too cumbersome to be implement. To circumvent the problem, compatible relations for Π_b and P/ε are devised with the assistance of References [14, 16] that depend nonlinearly on both the rotational and irrotational strains:

$$\Pi_b = C_v \frac{P}{\varepsilon}, \quad \frac{P}{\varepsilon} = C_v \zeta^2 \tag{16}$$

with

$$C_v = \frac{1}{2(1 + T_t S\sqrt{1+R^2})}, \quad \zeta = T_t S \max(1, R) \tag{17}$$

where $R = |W/S|$ is a dimensionless parameter that is very useful to characterize the flow. For instance, for a pure shear flow $R = 1$, whereas for a plane strain flow $R = 0$. It is appropriate to emphasize herein that introducing the auxiliary variables C_v and ζ, the proposed relation is constructed so as to meet the requirements of the equilibrium state: $P/\varepsilon \approx 1$ with $\Pi_b \approx 0.09$ (that are very close to the DNS data: $P/\varepsilon = 1$ and $\Pi_b \approx 0.095$) for the logarithmic region in a turbulent channel flow at $\zeta(R=1) \approx 3.3$ [22], and $P/\varepsilon \approx 1.9$ with $\Pi_b \approx 0.1$ for the homogeneous shear flow of Tavoularis and Corrsin (where $P/\varepsilon \approx 1.9$ and $\Pi_b \approx 0.11$) at $\zeta(R=1) \approx 6.0$ [23], respectively. Obviously, the anisotropic formulation augments the capacity of the two-equation

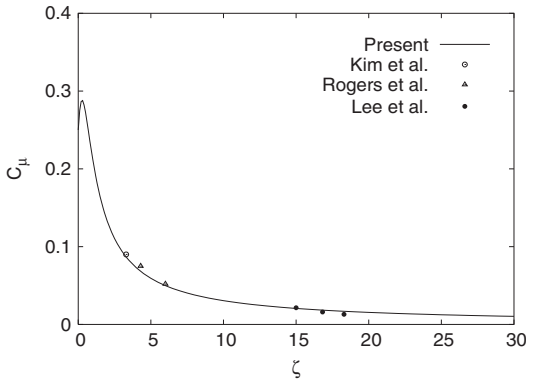

Figure 1. Distribution of C_μ as a function of shear parameter ζ.

model to account for nonequilibrium effects through the coefficient C_μ. Figure 1 shows the distribution of C_μ as a function of ζ. The C_μ distribution is in excellent agreement with various DNS data [24–26] for pure shear flows (i.e. homogeneous shear flows with $R=1$). The C_μ coefficient is reduced significantly with increasing ζ and maintained at a level that could mimic the complex turbulent flows.

The plane shear (i.e. homogeneous shear) flow, characterized by

$$S_{12}=S/2=S_{21}, \quad W_{12}=S/2=-W_{21} \tag{18}$$

is certainly an important example where the turbulence model needs to exhibit realizability. The flow field may either take the form of a boundary layer or a mixing layer [27]. In this situation, it is not difficult to justify that the present formulation produces nonnegative energy components.

The model realizability is further contrasted with the accelerated flow where turbulence can be strongly attenuated [27]. The turbulence attenuation is characterized by plane straining (where $R=0$), traditionally called stretching, rather than shear. Herein, the most pronounced attenuation of turbulence kinetic energy is the evolution of the component $\overline{u_1u_1}$ in the direction of a primary strain S_{11}. The fundamental stretching field together with the continuity equation for incompressible flow suggests that the limiting states are [27]: the 2-D stretching

$$S_{22}=-S_{11}(S_{33}=0), \quad S_{11}=S/2 \tag{19}$$

and the axisymmetric stretching

$$S_{22}=S_{33}=-S_{11}/2, \quad S_{11}=S/\sqrt{3} \tag{20}$$

The two cases in question are often associated with irrotational plane strain and axisymmetric contraction of the flow, having different implications on the model realizability. In both cases, the realizability principle applied to the present model implies that

$$\frac{\overline{u_1u_1}}{2k}=\frac{1}{3}-C_\mu T_t S_{11}\geqslant 0, \quad C_\mu=\frac{3(1+\eta^2)\alpha_1}{3+\eta^2} \tag{21}$$

The realizability principle pertaining to the 2-D plane strain and axisymmetric contraction states in Equation (21) requires

$$\frac{3C_\mu\zeta}{2} \leqslant 1, \quad \sqrt{3}C_\mu\zeta \leqslant 1 \tag{22}$$

where $\zeta = T_t S$. With attention restricted to this flow situation, Equation (16) can be recast as

$$\Pi_b^{1/2} = \frac{\zeta}{2(1+\zeta)}, \quad \frac{P}{\varepsilon} = \frac{\zeta^2}{2(1+\zeta)} \tag{23}$$

It can be easily verified that with Equation (23), relation (22) is satisfied at a moderate strain rate. However, if $\zeta \gg 1$, then $\zeta/(1+\zeta) \approx 1$. Therefore, $\Pi_b^{1/2} = 1/2$ and $P/\varepsilon = \zeta/2$. In this case, the model coefficients assume the following values:

$$\begin{aligned} \alpha_1 &= \frac{7}{12(1+\zeta)}, \quad \alpha_2 = \frac{3}{8\sqrt{2}(1+\zeta)} \\ \eta &= \frac{3\zeta}{8\sqrt{2}(1+\zeta)} = \frac{3}{8\sqrt{2}}, \quad C_\mu \approx \alpha_1 = \frac{7}{12(1+\zeta)} \end{aligned} \tag{24}$$

Consequently, with $C_\mu\zeta = 7/12$ one can certainly derive the conclusion that for $\zeta \gg 1$, the inequality (22) is marginally satisfied for a 3-D axisymmetric contraction of the flow. Above all, the present model does not exhibit unrealizable features at moderate (and compromisingly severe) strain rates.

2.2. *Near-wall modelling*

In the vicinity of the wall, the molecular viscosity effect is superior to the turbulent mixing, reflecting a strong anisotropic condition. Consequently, an important criterion regarding the appropriateness of the turbulence model is to represent the near-wall behaviour of turbulence quantities accompanied by a preferential damping of velocity fluctuations in the direction normal to the wall that reconciles the influence of wall proximity adequately.

The realizable time scale T_t can simply be defined as [14]

$$T_t = \sqrt{\frac{k^2}{\varepsilon^2} + C_T^2\frac{\nu}{\varepsilon}} = \frac{k}{\varepsilon}\sqrt{1 + \frac{C_T^2}{Re_\mathrm{T}}}, \quad Re_\mathrm{T} = \frac{k^2}{\nu\varepsilon} \tag{25}$$

where ν denotes the kinematic viscosity and Re_T is the turbulence Reynolds number. Equation (25) warrants that the eddy time scale never falls below the Kolmogorov time scale $C_T\sqrt{\nu/\varepsilon}$, dominant in the immediate neighbourhood of the solid wall. It prevents the singularity in the dissipation equation down to the wall. Alternatively, the turbulence time scale is k/ε at large Re_T but approaches the Kolmogorov limit $C_T\sqrt{\nu/\varepsilon}$ for $Re_\mathrm{T} \ll 1$. The empirical constant C_T associated with the Kolmogorov time scale is estimated as follows. In the viscous sublayer $k = y^2/(C_T^2\nu/\varepsilon)$, where the basic scale is the Kolmogorov time scale. Besides, the k equation reduces to $\nu\partial^2 k/\partial y^2 = \varepsilon$ as the wall is approached. Combining these relations provide $C_T = \sqrt{2}$. Obviously, the inclusion of T_t in the ε equation guarantees near-wall asymptotic consistency without resorting to *ad hoc* damping functions employed in many k–ε models [3].

In the vicinity of the wall, convection, turbulent diffusion and production approach zero very rapidly. Consequently, the ε equation in the near-wall region can be deduced in wall variables as follows:

$$\frac{\partial^2 \varepsilon^+}{\partial y^{+2}} - \frac{C_{\varepsilon 2}\varepsilon^+}{T_t^+} + \Pi_\varepsilon^+ = 0 \tag{26}$$

To analyse the wall turbulence phenomena, near-wall behaviours of the turbulent kinetic energy k, dissipation rate ε and characteristic time scale T_t are represented around $y^+ = 0$ as [11]

$$k^+ = a y^{+2} + b y^{+3} + c y^{+4} + \cdots \tag{27}$$

$$\varepsilon^+ = 2a + 4b y^+ + c_\varepsilon y^{+2} + \cdots \tag{28}$$

$$T_t^+ = C_T \sqrt{1/\varepsilon^+} = 1/\sqrt{a} + O(y^+) \tag{29}$$

where the coefficients $a = a(x^+, z^+)$, $b = b(x^+, z^+)$ and $c = c(x^+, z^+)$, given that y^+ is the normal distance from the wall surface.

Applying the expansions of k^+ and ε^+ to the various terms in Equation (26) yields

$$\frac{\partial \varepsilon^+}{\partial y^+} = 4b + 2c_\varepsilon y^+ + O(y^{+2}) \tag{30}$$

$$\frac{\partial^2 \varepsilon^+}{\partial y^{+2}} = 2c_\varepsilon + O(y^+) \tag{31}$$

$$\frac{C_{\varepsilon 2}\varepsilon^+}{T_t^+} = 2C_{\varepsilon 2} a\sqrt{a} + O(y^+) \tag{32}$$

$$\Pi_\varepsilon^+ = \frac{C_{\varepsilon 3}}{T_t^+}\left(\frac{\partial \sqrt{k^+}}{\partial y^+}\right)^2 = C_{\varepsilon 3} a\sqrt{a} + O(y^+) \tag{33}$$

The near-wall function Π_ε^+ is constructed such that its leading term can match the characteristics of other quantities in Equation (26). In principle, the dimensional form of the function can be given by

$$\Pi_\varepsilon = \frac{C_{\varepsilon 3}\mu}{T_t}\left(\frac{\partial \sqrt{k}}{\partial x_j}\right)^2 \tag{34}$$

where $C_{\varepsilon 3}$ is a model coefficient to be determined.

Substituting Equations (31)–(33) into Equation (26) provides for

$$C_{\varepsilon 3} = 2\left(C_{\varepsilon 2} - \frac{c_\varepsilon}{a\sqrt{a}}\right) \tag{35}$$

The DNS data for developed channel flows [28] supply the following information at the wall ($y^+ = 0$):

$$\left(\frac{\partial \varepsilon^+}{\partial y^+}\right)_w \approx -\frac{\varepsilon_w^+}{4}, \quad \left(\frac{\partial^2 \varepsilon^+}{\partial y^{+2}}\right)_w \approx \frac{\varepsilon_w^+}{8} \tag{36}$$

with $\varepsilon_w^+ = 0.165 - 0.22$ (where ε_w^+ is a function of the Reynolds number). Consequently, Equations (28), (30) and (31) contribute to: $b = -a/8$ and $c_\varepsilon = a/8$ with $2a = 0.165 - 0.22$. It seems likely that Equation (35) deems the values of $c_\varepsilon/(a\sqrt{a}) = 1/(8\sqrt{a})$ in the range of 0.3–0.5 at the wall. Since ε varies very rapidly near the wall, it is convenient to model $c_\varepsilon/(a\sqrt{a})$ instead of using selected values for $a = \varepsilon_w^+/2$. Recourse to the DNS data for channel flows, the following relation is developed that may replicate the behaviour of $c_\varepsilon/(a\sqrt{a})$ in the near-wall region:

$$\frac{c_\varepsilon}{a\sqrt{a}} = \beta, \quad \beta = C_\mu \zeta \tag{37}$$

where β resembles the anisotropy of turbulence (i.e. $\sqrt{b_{ij} b_{ij}}$), having $\beta \approx 0.3$ in the logarithmic region of a turbulent channel flow, where $T_t S = T_t W \approx 3.3$ [22]. Combining Equation (37) with Equation (35) gives

$$C_{\varepsilon 3} = 2(C_{\varepsilon 2} - \beta) \tag{38}$$

It is appropriate to emphasize herein that the proposed relation indubitably is conducive to allowing compatible changes in $C_{\varepsilon 3}$ that account for reproducing the level of turbulent kinetic energy (and therefore the wall dissipation rate since it is dependent on k) in the immediate vicinity of the wall. Apparently, the near-wall correction term Π_ε is prone to loose its influence outside the close proximity of the wall due to the molecular diffusion alone, recovering the parent high Reynolds number model. Sticking to the base equation for ε, So *et al.* [9] develop a similar type of near-wall correction term using Mathematica and imposing certain constraints. However, their model contains a constant coefficient for the proposed correction.

In the near-wall region, the turbulent kinetic energy equation can be simplified to [8]

$$\varepsilon^+ = \frac{\partial^2 k^+}{\partial y^{+2}} \approx 2\left(\frac{\partial \sqrt{k^+}}{\partial y^+}\right)^2 \tag{39}$$

Actually, the dimensional form of this relation is used to evaluate the wall boundary condition for ε. With Equation (27), an expansion equation is obtained from Equation (39) as

$$\varepsilon^+ = 2\left(\frac{\partial \sqrt{k^+}}{\partial y^+}\right)^2 = 2a + 4by^+ + 6cy^{+2} + \frac{y^{+2}(b + 2cy^+)^2}{2(a + by^+ + cy^{+2})} + \cdots \tag{40}$$

Comparing Equation (28) and Equation (40) generates the relation between the expansion coefficients:

$$c_\varepsilon = 6c + \frac{(b + 2cy^+)^2}{2(a + by^+ + cy^{+2})} \tag{41}$$

As the wall is approached (i.e. $y^+ = 0$), the relation reduces to

$$c = \frac{1}{6}\left(c_\varepsilon - \frac{b^2}{2a}\right) \tag{42}$$

Nevertheless, the previously determined wall values for the expansion coefficients (a, b, c_ε) imply that $c_\varepsilon \gg b^2/2a$. Therefore, $c_\varepsilon \approx 6c$, and Equations (27) and (28) can be recast as

$$k^+ = a y^{+2} + b y^{+3} + c y^{+4} + \cdots \tag{43}$$

$$\varepsilon^+ = 2a + 4b y^+ + 6c y^{+2} + \cdots \tag{44}$$

where

$$a = \frac{\varepsilon_w^+}{2}, \quad b = -\frac{a}{8}, \quad c = \frac{c_\varepsilon}{6} = \frac{a}{48} \tag{45}$$

A comparative assessment made of the present results and those of DNS data at $Re_\tau = u_\tau \delta/\nu = 180$ and 395, respectively, is shown in Figures 2 and 3. Herein, u_τ is the friction velocity and δ denotes the channel half-width. In these figures the abbreviation SSGZ stands for the model of So *et al.* [9]. Although, the DNS wall values for ε^+ are used to evaluate the coefficients (a, b, c), the agreement between the present k^+ and ε^+ expansions, and DNS data is excellent in the near-wall region $0 < y^+ < 5$. It seems likely that the SSGZ expansion coefficients are tuned to the channel flow at $Re_\tau = 395$.

The damping function included in Equation (8) is chosen pragmatically as

$$f_\mu = 1 - \exp(-R_\lambda), \quad R_\lambda = \frac{Re_y^{1.5}}{2(\zeta + Re_T)} \tag{46}$$

where $Re_y = y\sqrt{k}/\nu$, another Reynolds number associated with the turbulence modelling. A plot of $C_\mu f_\mu$ against the DNS data [28] for a fully developed turbulent channel flow is shown in Figure 4 and good correlation is obtained. The result of the SSGZ model is also included in the figure for comparison. The empirical function f_μ is valid in the whole flow field, including the viscous sublayer and the logarithmic layer. In the region close to the wall, the Reynolds stress $-\overline{uv} \sim y^3$ and $k \sim y^2$. To preserve the correct cubic power-law behaviour of $-\overline{uv}$, the damping function (herein the product $C_\mu f_\mu$) needs to increase proportionally to y^{-1} in the near-wall region. Equation (46) confirms that as $Re_T > \zeta$, $C_\mu f_\mu \sim y^{-1}$ in close proximity to the wall. As evinced by Figure 4 in comparison with the DNS data, the adopted form of $C_\mu f_\mu$ reproduces the asymptotic limit involving the distinct effects of LRN and wall proximity. The product $C_\mu f_\mu \approx 0.09$ (the standard choice for $C_\mu = 0.09$, pertaining to the linear k–ε model) remote from the wall to ensure that the model is compatible with the standard k–ε turbulence model. The use of $R_\lambda = R_\lambda(Re_y, Re_T)$ confronts the singularity at neither the separating nor the reattaching point in contrast to the adoption of $y^+ = u_\tau y/\nu$. Consequently, the model is applicable to separated and reattaching flows.

The budgets of k and ε from the DNS data suggest that the role of turbulent diffusion in the near-wall region is substantial. Accordingly, the coefficients $\sigma_{(k,\varepsilon)}$ are modelled, rather than being assigned constant values (unlike the commonly adopted practice with $\sigma_k = 1.0$,

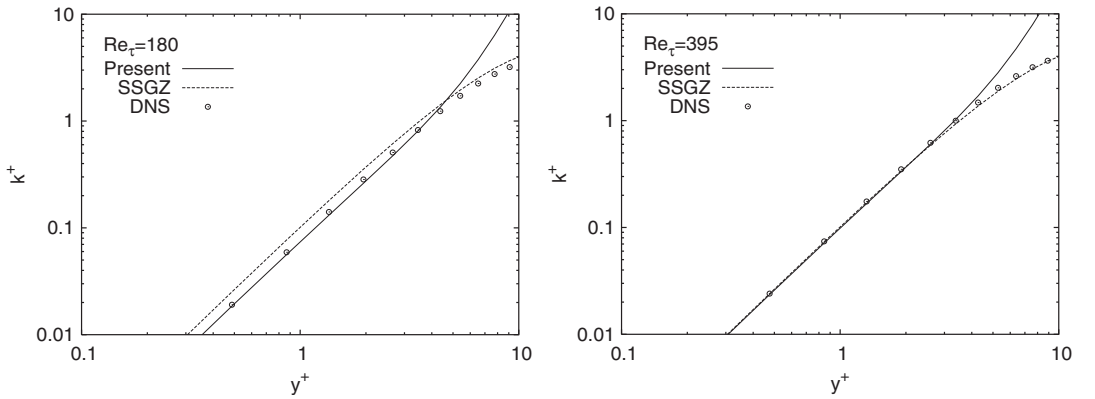

Figure 2. Comparison of the asymptotic behaviour of k^+ with DNS data.

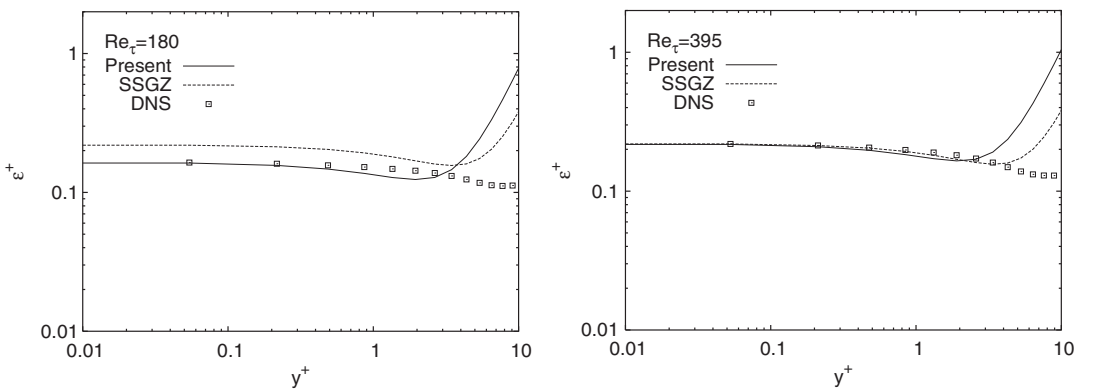

Figure 3. Comparison of the asymptotic behaviour of ε^+ with DNS data.

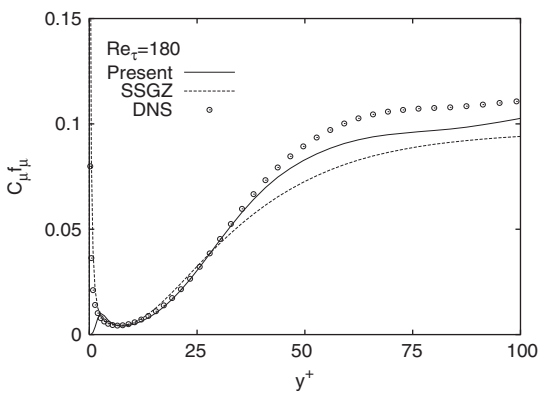

Figure 4. Variations of eddy viscosity coefficient with wall distance in channel flow.

and $\sigma_\varepsilon = 1.3$):

$$\sigma_\varepsilon = \beta + f_\mu, \quad \sigma_k = \frac{\sigma_\varepsilon}{1 - C_\mu f_\mu} \tag{47}$$

The model coefficients $\sigma_{(k,\varepsilon)}$ are developed such that sufficient diffusion is obtained in the vicinity of the wall and in the core region of the flow $\sigma_k/\sigma_\varepsilon > 1$ to eliminate the common drawback where the turbulent diffusion of k overwhelms the diffusion of ε with $\sigma_k < \sigma_\varepsilon$ [5]. Note that the parameters/coefficients associated with the turbulent Prandtl numbers $\sigma_{(k,\varepsilon)}$ have the values in the range from 0 to 1. For instance, $0 < f_\mu \leqslant 1$, $0 < C_\mu < 0.5$ and $0 < \beta < 0.5$. Therefore, the violation of realizability and the occurrence of singularity problem in Equation (47) are avoided.

The transport equations for k and ε are subjected to the following boundary conditions at solid walls:

$$k_w = 0, \quad \varepsilon_w = 2\nu \left(\frac{\partial \sqrt{k}}{\partial y} \right)^2 \approx 2\nu \frac{k}{y^2} \tag{48}$$

To avoid numerical instability, the approximation for ε_w is applied at the first grid node neighbouring the wall, rather than on the wall itself. This requires normal distance from a wall to the nearest grid point, which is unambiguous and readily available. The validity of Equation (48) necessitates that the grid system is fine enough to produce the near-wall limiting behaviour.

3. COMPUTATIONS

To ascertain the efficacy of the proposed model, a few applications to 2-D turbulent flows consisting of a fully developed channel flow, an asymmetric plane diffuser flow and a plane U-duct flow are considered. For a comparison purpose, calculations from the SSGZ model [9] are included. The possible reasoning for the choice of the SSGZ model is that it contains a similar type of near-wall correction term having a constant coefficient. Furthermore, it uses the Kolmogorov velocity scale in the eddy viscosity damping function to account for near-wall effects. Therefore, the SSGZ model is supposed to evaluate the combined effects of LRN and near-wall turbulence with reasonable accuracy. However, compared with the SSGZ model, the new model is additionally sensitized to nonequilibrium and anisotropic effects.

A cell centred finite-volume scheme combined with an artificial compressibility approach is employed to solve the flow equations [29, 30]. A fully upwinded second-order spatial differencing is applied to approximate the convective terms. Roe's [31] damping term is used to calculate the flux on the cell face. A diagonally dominant alternating direction implicit (DDADI) time integration method [32] is applied for the iterative solution to the discretized equations. A multigrid method is utilized for the acceleration of convergence [33]. The basic implementation of the artificial compressibility method and associated features are described in References [29, 30].

A variable grid spacing is used to resolve the sharp gradient in near-wall regions. Grid densities are varied to ensure the grid independence of the numerical results. It is found that the solution is not very sensitive to the number of grid points as long as there are two points

in $y^+ < 1.5$. In the computations that follow, convergence is judged by monitoring the root-mean-square residuals of flow variables. The solution is taken as having converged when all residuals are of the order 10^{-4} or less.

3.1. Channel flow

The computation is carried out for a fully developed turbulent channel flow at $Re_\tau = 180$ for which turbulence quantities are attainable from the DNS data [28]. The calculation is conducted in the half-width of the channel, imposing periodic boundary conditions, except for the pressure, pertaining to the upstream and downstream boundaries. The computation involving a 64×48 nonuniform grid refinement is considered to be sufficiently accurate to describe the flow characteristics. For this case, the length of the computational domain is 32δ. To ensure the resolution of the viscous sublayer the first grid node near the wall is placed at $y^+ \approx 0.3$. Comparisons are made by plotting the results in the form of $u^+ = u/u_\tau$, $k^+ = k^+/u_\tau^2$, $\overline{uv}^+ = \overline{uv}/u_\tau^2$ and $\varepsilon^+ = \nu\varepsilon/u_\tau^4$ versus y^+.

Figure 5 shows the velocity profiles for different models. The prediction of the present model agrees well with the DNS data. The SSGZ model slightly underestimates the mean velocity profile in the outer layer. Profiles of turbulent shear stresses are displayed in Figure 6. Agreement of both model predictions with the DNS data seems to be satisfactory.

Further examination of the model performances is directed to the k^+ profiles as portrayed in Figure 7 for the near-wall region. As is evident, the present model prediction is in broad accord with the SSGZ model and DNS data. Figure 8 exhibits the profiles of ε^+ from the two computations. The present as well as the SSGZ model provides a maximum ε^+ at the wall which is more in line with the experimental and DNS data.

3.2. Asymmetric plane diffuser flow

To validate the performance in complex separated and reattaching turbulent flows, the present model is applied to the flow in an asymmetric diffuser with an opening angle of 10°, for which measurements are available [34]. The expansion ratio of 4.7 is sufficient to produce a separation bubble on the deflected wall. Hence the configuration provides a test case for smooth, adverse pressure driven separation. The entrance to the diffuser consists of a plane

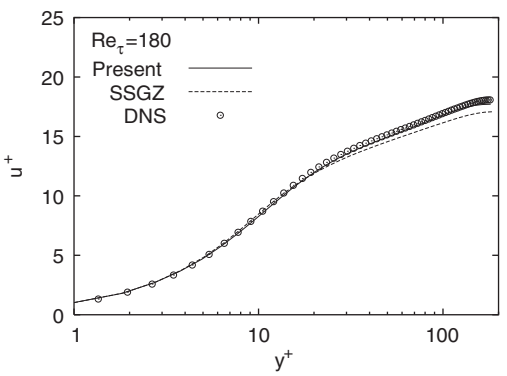

Figure 5. Mean velocity profiles of channel flow.

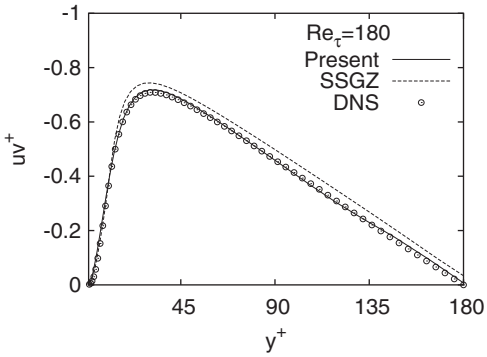

Figure 6. Shear stress profiles of channel flow.

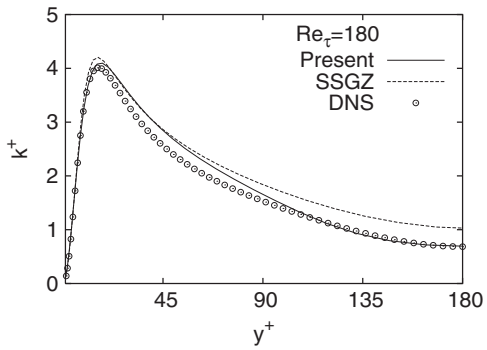

Figure 7. Turbulence kinetic energy profiles of channel flow.

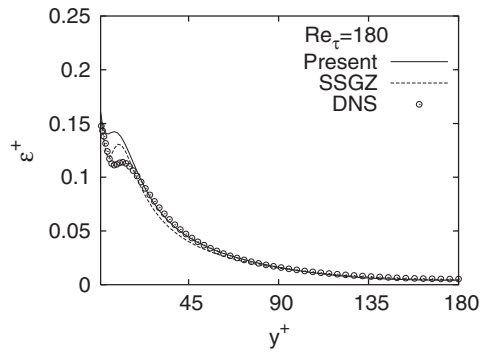

Figure 8. Dissipation rate profiles of channel flow.

channel to invoke fully developed flow with $Re = 2.0 \times 10^4$ based on the centreline velocity U_{ref} and the inlet channel height h. Computations involving a 120×72 nonuniform grid resolution are considered to be accurate to describe the flow characteristics. The length of

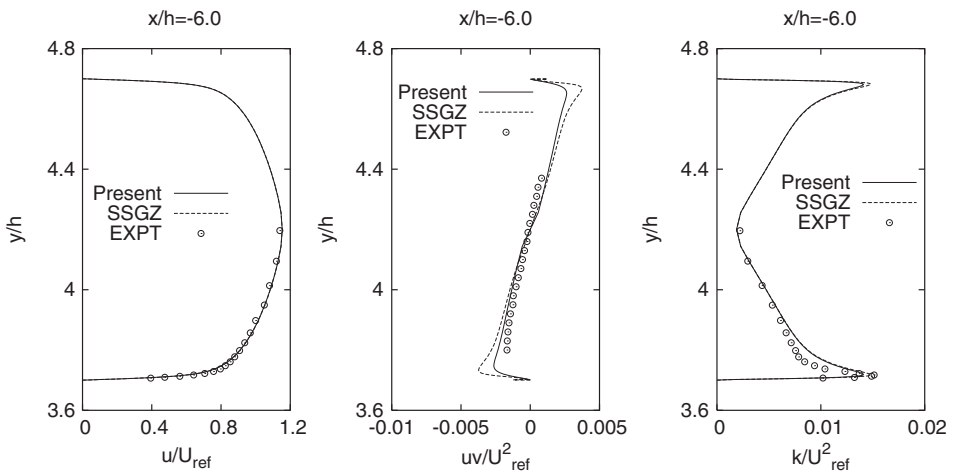

Figure 9. Inlet profiles for diffuser flow.

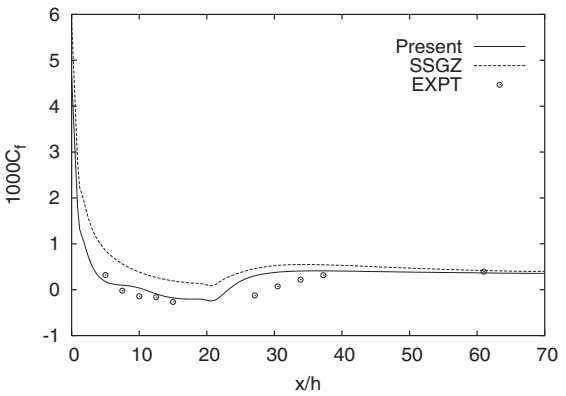

Figure 10. Skin friction coefficient of diffuser flow along deflected bottom wall.

the computational domain is $76h$. The thickness of the first cell remains below one in y^+ units on both the deflected and flat walls. Profiles of mean velocity, shear stress and turbulent kinetic energy at inlet are presented in Figure 9. The present and SSGZ models ensure close adherence to the experimental data.

Figure 10 portray the predicted skin friction coefficients C_f. The performance of the present model evinces an encouraging qualitative agreement with measurements. As is observed, the SSGZ model predicts C_f distribution with an overshoot along the deflected bottom wall and gives no flow separation. Apparently, this ambiguous prediction regarding the SSGZ model demands a higher value for the proposed near-wall correction in the ε equation to render the model results compatible with the experiment.

Figure 11 exhibits the mean velocity profiles at three representative positions. The performance of both models in predicting the velocity profiles is distinguishable. Unlike the SSGZ

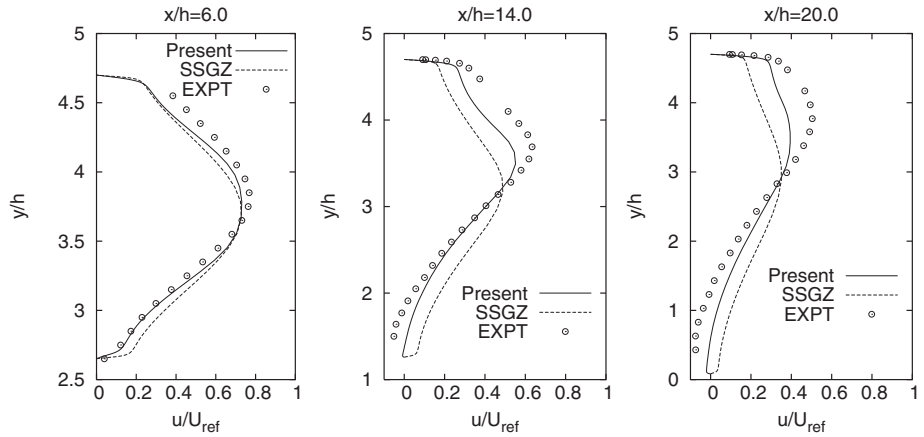

Figure 11. Mean velocity profiles at selected locations for diffuser flow.

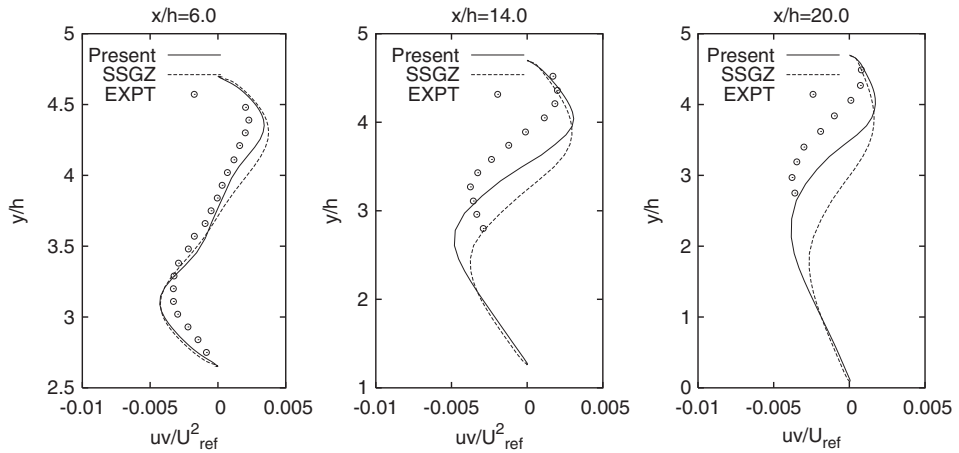

Figure 12. Shear stress profiles at selected locations for diffuser flow.

model, the present model predicts some anisotropy of turbulence due to the variation of C_μ in the eddy viscosity formulation, and hence yields results in better agreement with the data. However, compared with the experiment both models tend to gradually underpredict the peak for u-profile toward the outlet of the diffuser. Comparisons are extended to the distributions of Reynolds shear stress and the corresponding turbulent kinetic energy at different x/h locations, as displayed in Figures 12 and 13. Since the $\overline{ww}$ component is not measured in the experiment, the usual approximation $k \approx 3/4(\overline{uu} + \overline{vv})$ is employed. A closer inspection of the distribution indicates that the present model predictions are in a broad agreement with the experimental data. The SSGZ has noticeable discrepancies with the measured data farther downstream. In fact, the flow inside the diffuser is characterized by strongly anisotropic turbulence. The inaccurately predicted mean velocity and turbulence profiles may largely be

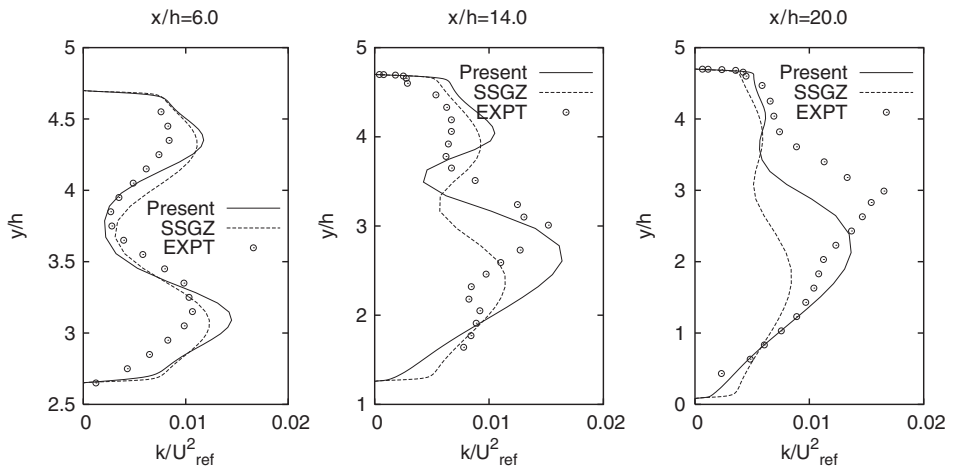

Figure 13. Kinetic energy profiles at selected locations for diffuser flow.

Figure 14. Computational grid for U-duct flow.

attributed to the models used which, by their linear nature, are unable to appropriately respond to strong anisotropy.

3.3. *Plane U-duct flow*

To further evaluate the performance, the model is applied to simulate the flow in a plane U-duct with strong streamline curvature effects. The computations are conducted corresponding to the experimental case with $Re = 10^6$, based on the channel height $h = 3.81$ cm and reference velocity $U_{\text{ref}} = 31.8$ m/s [35, 36]. The turn has an inner radius of $r_{\text{i}} = 1.91$ cm and an outer radius of $r_{\text{o}} = 5.72$ cm. The finest grid employed is 288×160 and extends from $x/h = -4$ upstream of the bend to $x/h = 12$ downstream. The maximum height of the first near-wall grid node is at $y^+ < 1.0$. The computational grid is shown in Figure 14. The inlet boundary conditions are approximated from the experimental data, as depicted in Figure 15. A coarser grid 144×80 is used to investigate grid sensitivity. However, no significant differences are found between the coarse and fine grid results.

The predicted and experimental profiles of the streamwise velocity, shear stress and turbulent kinetic energy are shown in Figures 16–18, respectively. At station $\theta = 0^\circ$ ($x/h = 0$, where the bend begins), both models predicts the mean velocity in good agreement with each other and with experiment. The flow undergoes rapid acceleration near the inner wall and deceleration

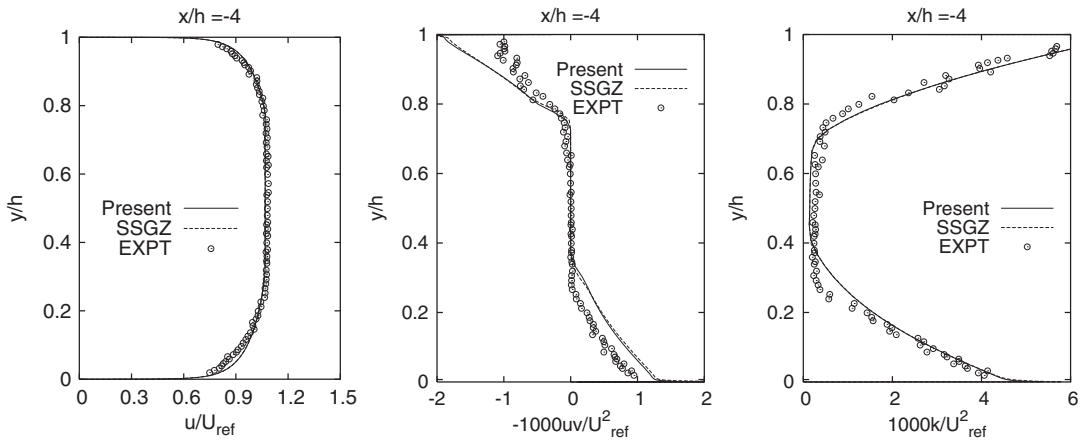

Figure 15. Profiles at inlet for U-duct flow.

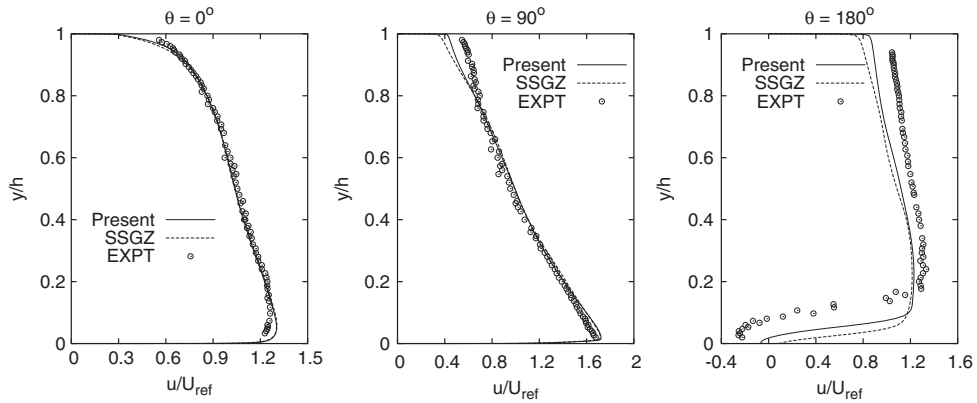

Figure 16. Velocity profiles at selected locations for U-duct flow.

near the outer wall. The curvature effect on turbulence can be clearly observed from the experimental data. The convex curvature together with a large flow acceleration strongly attenuates the turbulence shear stress and kinetic energy near the inner wall. The present model provide good predictions for $-\overline{uv}$ near the convex/concave wall. However, the SSGZ model overpredicts the shear stress magnitudes significantly near both walls. For the kinetic energy profiles, both models yield similar results that agree with the measured data at the convex wall, but underpredict the magnitude of turbulence kinetic energy near the concave wall to a large extent.

As the flow reaches the $\theta = 90^\circ$ position halfway around the bend, the curvature of the bend affects the turbulence profoundly. The turbulence is damped near the convex wall, whereas turbulence enhancement occurs near the concave wall. Both models predict similar velocity profiles having reasonable agreement with experiment, although the velocity magnitude near

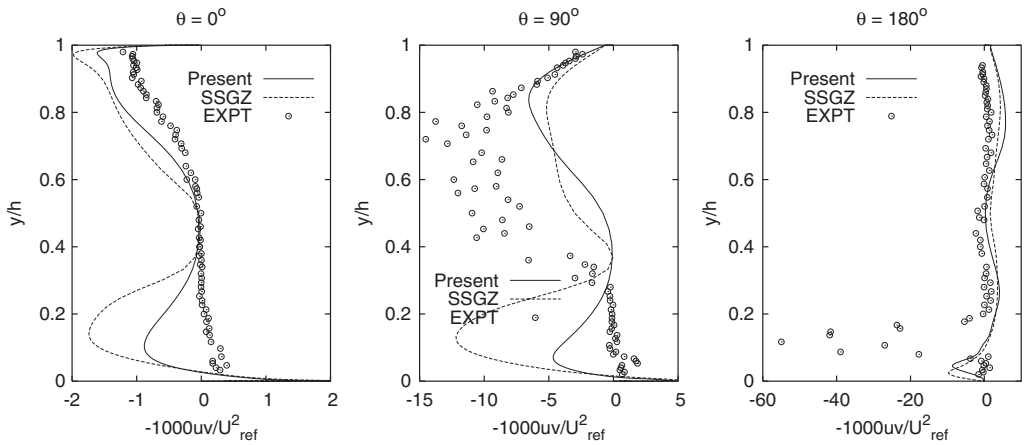

Figure 17. Shear stress profiles at selected locations for U-duct flow.

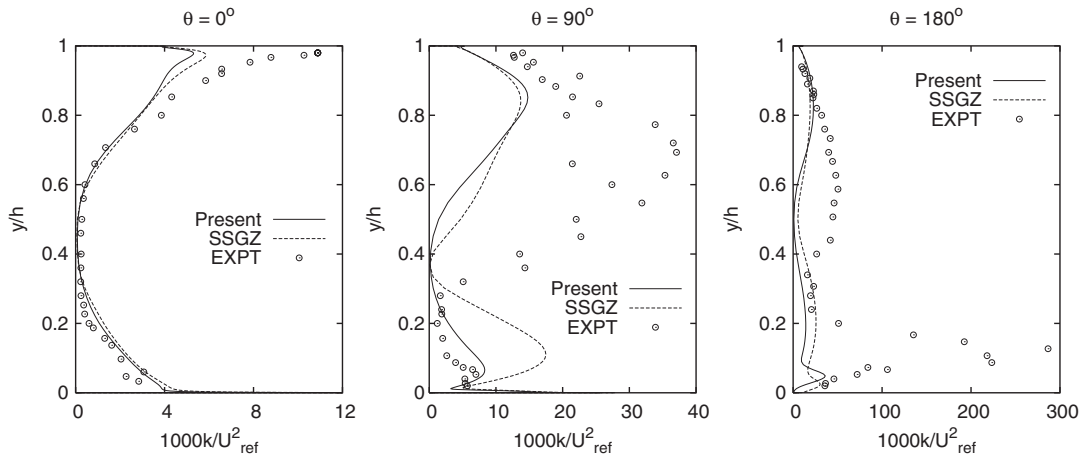

Figure 18. Kinetic energy profiles at selected locations for U-duct flow.

the outer wall is underpredicted. The SSGZ model with a constant C_μ is not actively sensitive to the curvature effect, overpredicting/underpredicting the shear stress and kinetic energy levels at the convex/concave surface. In strong contrast, the present model with a variable C_μ shows improved predictions of $-\overline{uv}$ and k near both walls, in better agreement with the experiment.

In fact, the flow envisages an adverse pressure gradient on the inner wall and a favourable pressure gradient on the outer wall downstream of $\theta = 90°$ [37]. Due to the severe adverse pressure gradient, as well as highly diminished turbulent shear stress, the boundary layer separates in the experiment around $\theta = 150°$ on the convex wall and extends to $x/h = 1.0$–1.5 downstream of the end of bend. The velocity profiles predicted by the present and SSGZ models at station $\theta = 180°$ agree well with the data. Nevertheless, there is a remarkable

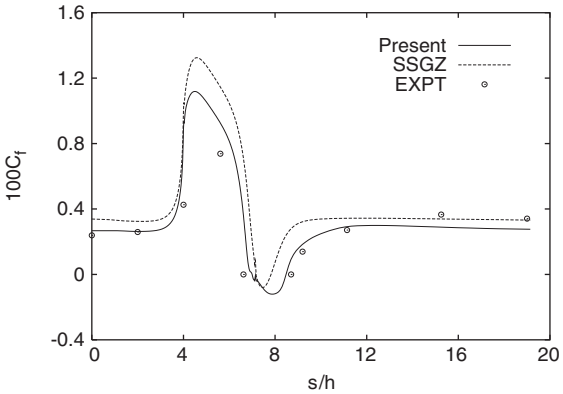

Figure 19. Inner surface skin friction coefficient for U-duct flow.

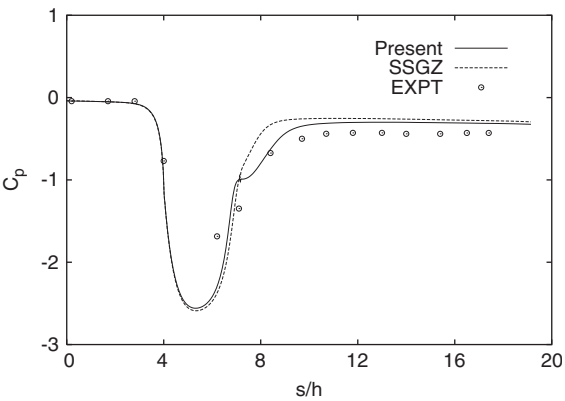

Figure 20. Inner surface pressure coefficient for U-duct flow.

discrepancy between the numerical and experimental results in the turbulence quantities at the end of bend. The measured data show a very strong peak in the turbulent kinetic energy and shear stress profiles at the convex surface, which is not captured by any model. This large peak values probably result from large unsteadiness of the separation bubble, as reported in the experiment.

Computed and experimental friction coefficients C_f on the inner wall are plotted in Figure 19. The s signifies the distance of the channel centreline from the U-duct inlet. As is observed, the present model result is close to that of experimental data. It nearly captures the separation and reattachment points, having comparable separation length in good agreement with the data. On the other hand, the SSGZ model yields a significantly smaller region of separation in comparison with the data. The static pressure coefficient C_p along the inner wall is shown in Figure 20. On average, both models predict the pressure level downstream of the bend in good agreement with the experiment. However, the predicted C_p regarding the SSGZ model near the bend exit is not accurate because it induces too quick a recovery after

reattachment. The prediction by the present model seems to be a good compromise with the experiment.

4. CONCLUSIONS

The proposed turbulent model is susceptible to the near-wall and low-Reynolds number effects emanating from the physical requirements. The potential importance of the damping functions is conspicuous. The new eddy viscosity formulation depends nonlinearly on both the mean strain rate and vorticity invariants, and ensures realizability. The anisotropic production in the dissipation equation is accounted for substantially by adding a near-wall correction, leading to a reduced level of turbulence generation in nonequilibrium flow regions. Consequently, the model is capable of evaluating the flow cases entangling separation and reattachment. Contrasting the predicted results with measurements demonstrates that the present model offers considerable improvement over the constant C_μ model.

NOMENCLATURE

b_{ij}	Reynolds stress anisotropy
C_f	friction coefficient
C_μ	eddy viscosity coefficient
e	specific internal energy
f_μ	viscous damping function
F, G	flux vectors in x- and y-directions
h	channel height
$\mathbf{i}, \mathbf{j}$	unit vectors in Cartesian coordinate system
k	turbulent kinetic energy; heat conductivity
p	static pressure
P	production of turbulent kinetic energy
Pr	Prandtl number
q	heat flux
Q	source term
S	mean strain rate
t	time
T	temperature
T_t	realizable time scale
U	vector of the conservative variables
u, v	velocity components in x- and y-directions
W	mean vorticity
x, y	Cartesian coordinates
y^+	nondimensional normal distance from the surface

Greek letters

β	turbulent anisotropy
δ	half-width of the channel

δ_{ij}	Kronecker's delta
ε	turbulent dissipation
μ, μ_T	laminar and eddy viscosities
ν	molecular kinematic viscosity
ρ	density
Π_ε	near-wall correction
σ	turbulent Prandtl number
τ	shear stress

Subscripts

T	turbulent condition
ref	reference condition
v	viscous part

REFERENCES

1. Jones WP, Launder BE. The calculation of low-Reynolds number phenomena with a two-equation model of turbulence. *International Journal of Heat and Mass Transfer* 1973; **16**:1119–1130.
2. Chien K-Y. Predictions of channel and boundary layer flows with a low-Reynolds number turbulence model. *AIAA Journal* 1982; **20**:33–38.
3. Patel VC, Rodi W, Scheuerer G. Turbulence models for near-wall and low Reynolds number flow: a review. *AIAA Journal* 1985; **23**:1308–1319.
4. Mansour NN, Kim J, Moin P. Near-wall k–ε turbulence modeling. *AIAA Journal* 1989; **27**:1068–1073.
5. Nagano T, Tagawa M. An improved k–ε model for boundary layer flows. *Journal of Fluids Engineering* 1990; **112**:33–39.
6. Durbin PA. Near-wall turbulence closure modeling without damping functions. *Theoretical and Computational Fluid Dynamics* 1991; **3**:1–13.
7. Yang Z, Shih TH. New time scale based k–ε model for near-wall turbulence. *AIAA Journal* 1991; **29**: 1337–1340.
8. Nagano Y, Kondoh M, Shimada M. Multiple time scale turbulence model for wall and homogeneous flows based on direct numerical simulations. *International Journal of Heat and Fluid Flow* 1997; **18**:346–359.
9. So RMC, Sarkar A, Gerodimos G, Zhang J. A dissipation date equation for low-Reynolds number and near-wall turbulence. *Theoretical and Computational Fluid Dynamics* 1997; **9**:47–63.
10. Goldberg U, Apsley D. A wall-distance-free low RE k–ε turbulence model. *Computer Methods in Applied Mechanics and Engineering* 1997; **145**:227–238.
11. Hwang CB, Lin CA. Improved low-Reynolds number k–$\tilde{\varepsilon}$ model based on direct numerical simulation data. *AIAA Journal* 1998; **36**:38–43.
12. Rahman MM, Siikonen T. Improved low-Reynolds-number k–$\tilde{\varepsilon}$ model. *AIAA Journal* 2000; **38**:1298–1300.
13. Rahman MM, Siikonen T. Low-Reynolds-number k–$\tilde{\varepsilon}$ model with enhanced near-wall dissipation. *AIAA Journal* 2002; **40**:1442–1464.
14. Rahman MM, Siikonen T. Near-wall turbulence modelling with enhanced dissipation. *International Journal for Numerical Methods in Fluids* 2003; **42**:979–997.
15. Rahman MM, Siikonen T. A two-equation model with relevance to near-wall turbulence. *Far East Journal of Applied Mathematics* 2004; **17**:1–26.
16. Rahman MM, Siikonen T. Low-Reynolds number k–ε model for near-wall flow. *International Journal for Numerical Methods in Fluids* 2005; **47**:325–338.
17. Lumley JL. Computational modeling of turbulent flows. *Advances in Applied Mechanics* 1978; **18**:124–176.
18. Pope SB. A more general effective viscosity hypothesis. *Journal of Fluid Mechanics* 1975; **72**:331–340.
19. Gatski TB, Speziale CG. On the explicit algebraic stress models for complex turbulent flows. *Journal of Fluid Mechanics* 1993; **254**:59–78.
20. Shih T-H, Zhu J, Lumley JL. A new Reynolds stress algebraic equation model. *Computer Methods in Applied Mechanics and Engineering* 1995; **125**:287–302.
21. Girimaji SS. Fully explicit and self-consistent algebraic Reynolds stress model. *Theoretical and Computational Fluid Dynamics* 1996; **8**:387–402.
22. Kim J. Personal communication, 1990.

23. Tavoularis S, Corrsin A. Experiments in nearly homogeneous turbulent shear flow with a uniform mean temperature gradient. *Journal of Fluid Mechanics*, *Part I* 1981; **104**:311–347.
24. Kim J, Moin P, Moser R. Turbulence statistics in fully developed channel flow at low Reynolds number. *Journal of Fluid Mechanics* 1987; **177**:133–166.
25. Lee MJ, Kim J, Moin P. Structure of turbulence at high shear rate. *Journal of Fluid Mechanics* 1990; **216**: 561–583.
26. Rogers MM, Moin P. The structure of the vorticity field in homogeneous turbulent flows. *Journal of Fluid Mechanics* 1987; **176**:33–66.
27. Rung T, Thiele F, Fu S. On the realizability on nonlinear stress–strain relationships for Reynolds stress closures. *Flow*, *Turbulence and Combustion* 1999; **60**:333–359.
28. Mansour NN, Kim J, Moin P. Reynolds-stress and dissipation-rate budgets in a turbulent channel flow. *Journal of Fluid Mechanics* 1988; **194**:15–44.
29. Rahman MM, Rautaheimo P, Siikonen T. Numerical study of turbulent heat transfer from a confined impinging jet using a pseudo-compressibility method. In *Second International Symposium on Turbulence*, *Heat and Mass Transfer*, Delft, The Netherlands, Hanjalic KK, Peeters TWJ (eds). Delft University Press: Delft, 1997; 511–520.
30. Rahman MM, Siikonen T. An artificial compressibility method for incompressible flows. *Numerical Heat Transfer*, *Part B* 2001; **40**:391–409.
31. Roe PL. Approximate Riemann solvers, parameter vectors, and difference schemes. *Journal of Computational Physics* 1981; **43**:357–372.
32. Lombard C, Bardina J, Venkatapathy E, Oliger J. Multi-dimensional formulation of CSCM—an upwind flux difference eigenvector split method for the compressible Navier–Stokes equations. *Sixth AIAA Computational Fluid Dynamics Conference*, *AIAA Paper 83-1895-CP*, 1983; 649–664.
33. Jameson A, Yoon S. Multigrid solution of the Euler equations using implicit schemes. *AIAA Journal* 1986; **24**:1737–1743.
34. Buice C, Eaton JK. Experimental investigation of flow through an asymmetric plane diffuser. *Report TSD-107*, Department of Mechanical Engineering, Thermoscience Division, Stanford University, California, CA, 1997.
35. Monson DJ, Seegmiller HL, McConnaughey PK, Chen YS. Comparison of experiment with calculations using curvature-corrected zero and two-equation turbulence models for a two-dimensional U-duct. *AIAA Paper 90-1484*, 1990.
36. Monson DJ, Seegmiller HL. An experimental investigation of subsonic flow in a two-dimensional U-duct. *NASA TM 103931*, 1992.
37. Luo J, Lakshminarayana B. Prediction of strongly curved turbulent duct flows with Reynolds stress model. *AIAA Journal* 1997; **35**:91–98.

